scientific reports

OPEN

Biomimetic design and impact simulation of Al$_2$O$_3$/Al composite armor based on armadillo shell

Fulong Zhang[1], Peng Zhu[1], Ping Lu[2], kai Qian[1], Shuangyu Liu[1✉] & Liyan Wang[1]

The advancement of lightweight protective armors holds critical importance for enhancing the maneuverability and combat capabilities of helicopters. Leveraging insights from bionics, it provides a new idea for high-performance armor design. In this study, a new type of composite armor was designed by referring to the structural characteristics of hard phase-protection, soft phase-buffering of unitization armadillo shell. Through the numerical study, the anti-ballistic performance of armor with varying thickness ratios of the dense ceramic layer to the interpenetrating layer is obtained, and the influence of different structures of armor on the anti-ballistic performance is analyzed. The results show that compared with the traditional laminated composite armor, the Al$_2$O$_3$/Al biomimetic composite armor not only improves the separation phenomenon caused by wave impedance mismatch, but also greatly improves the speed drop in resisting high-speed and penetrating bullets. When the thickness ratio is 2:1, the armor has higher ballistic protection performance.

Armor constitutes a pivotal defense mechanism to safeguard weapon systems' functionality and personnel safety, which has seen its relevance markedly increase within contemporary combat scenarios[1]. In the context of military helicopter operations, vulnerability to ground-fired ordnance necessitates an armoring solution that balances enhanced reliability, superior protective attributes, maintenance simplicity, and flexibility[2–4]. The gamut of armor materials predominantly encompasses metals, composites, and ceramic matrices[5,6]. Compared to metal protective materials[1] and flexible composite materials[7], ceramics are imbued with advantageous properties like diminished weight, considerable hardness, and robust resistance to compressive forces[8], making them favorable candidates for novel armoring solutions. Nevertheless, given the strides in ballistics fostering lighter materials with augmented protective merits, singular-material solutions fall short of current defense standards. However, due to the increase in protective needs, single material can no longer meet the requirements. Ceramic/metal composite material[9,10] combines the dual characteristics of ceramic and metal, which greatly improves the armor protection ability.

The laminated composite structure in ceramic/metal composite armor cleverly combines the high strength of ceramic materials with the elasticity of metals through adhesive bonding technology. However, this method produces significant variations in the hardness, elastic modulus, density, and toughness at the adhesive interface, ultimately leading to impedance mismatch and localized stress enhancement between the various layers[11,12]. A far graver concern is the potential for large-scale cracking and delamination at the adhesive junction between the facing and back plates[13,14]. To address these vulnerabilities, interpenetrating phase composites (IPCs) have been postulated. These materials manifest a synergistic amalgam of strength, ductility, and rigidity, augmented by exceptional wear resistance and a versatility in microstructural customization and processing paradigms[15,16]. The gradient structure designed by Wang and colleagues[17] adeptly moderates the impedance mismatch and counters delamination, while the altered toughness gradient and energy dissipation trends suppress crack propagation within B$_4$C-rich regions, thus effectively absorbing substantive energy and alleviating damage. In separate research, Chao et al.[18] prepared a B$_4$C/AA2024 composite gradient architecture spanning 70–47–25 vol%. The resultant material demonstrated diminished damage diameters by 9.6 mm relative to the uniform distribution of 70 vol% B$_4$C/AA2024 composite. Kota and associates[19] engineered interpenetrating ceramic–metal composites, achieving a hardness more than 50% greater than the base Al–Si alloy, with finer pore composites exhibiting

[1]College of Mechanical Engineering, Yancheng Institute of Technology, Yancheng 224051, China. [2]College of Automotive Engineering, Yancheng Institute of Technology, Yancheng 224051, China. ✉email: liushuangyu@ycit.edu.cn

even greater hardness improvements. Prasanth and his team[20] observed that crack initiation began from the C_4 structural frame, particularly in the SiC foam structure.

While IPCs exhibit superior performance compared to laminated composite structures, with better ballistic resistance at an equivalent areal density. But the traditional methods for preparing ceramic frameworks for IPCs, such as foaming and freeze casting, have issues of uncontrollability and simple structures. Consequently, IPCs prepared using these methods exhibit step changes in material properties along the penetration direction. The impedance mismatch within these structures prevents the gradient attenuation of stress waves upon high-velocity projectile penetration, resulting in significant damage and failure of the ceramic and metal phases from a single penetration impact. As a result, the ability to withstand subsequent impacts is further compromised. In recent years, the advancement of additive manufacturing technology has led to the realization of controlled design and precise production of ceramic frameworks, making them a viable option. The controlled and precision-driven development of ceramic frameworks, enabled by the advances in additive manufacturing, is demonstrably realized by Lu et al[21]. Research has demonstrated[22] that when IPCs are adhesively bonded to dense alumina ceramics, significant deviation of the penetrating projectile is observed, resulting in a reduced depth of penetration (DoP). However, a connection between the dense ceramic layer and the IPC layer is still required. The impedance mismatch at the interface remains unresolved, and the bond strength between aluminum and the ceramic layer presents even greater challenges.

Moreover, modularizing the integral ceramic/metal armor structure has reduced the upgrade and maintenance cycle and cost of the armor[23]. The concept of biomimicry provides compelling directions for the innovative design of advanced armor systems[24–26]. Numerous animals, including armadillos, pangolins, fish, and snakes, feature scales that meld defense and flexibility[27]. The armadillo's shell has evolved to bolster its strength and energy absorption, thereby enhancing bodily protection[28]. These energy-dissipating constructs have stimulated initiatives to emulate their mechanics in developing armor materials that absorb impact through plastic deformation[29].

In conclusion, this study proposes a novel bio-inspired ceramic/metal composite armor, integrating the holistic structure of armadillo shells, unit elements of the carapace, and triply periodic minimal surface structures to form a monolithic dense ceramic and ceramic framework formed in one body.

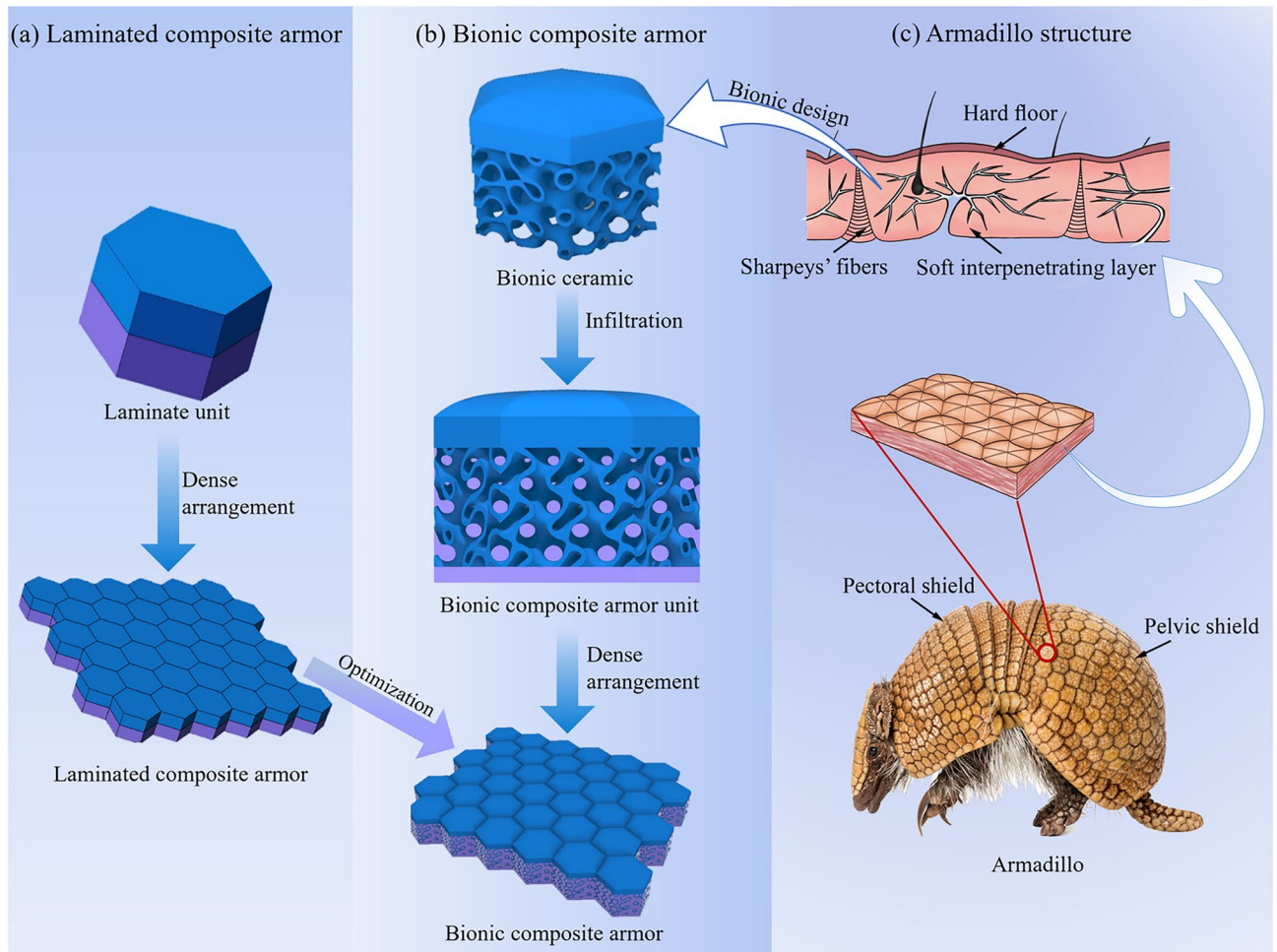## Biomimetic design of Al_2O_3/Al composite armor
Feasibility analysis

The above-cited literature has proved the feasibility and effectiveness of bionic armor and unitization through scientific research, while the positive effect of TPMS on ballistic resistance has yet to be studied. Guo et al.[30] conducted finite element analysis and verified the ballistic performance of laminate structure and honeycomb structure armor. They found that the addition of honeycomb structure reduced the impact resistance of a single hit, but did not reduce the ability to resist a second hit. In addition, our research team discovered that TPMS-infused composites exhibited lower levels of local stress concentration, which gave them higher strength and ductility compared to honeycomb composites[31]. The ultimate compressive strength of the Gyroid curved composite material is 264 MPa, which is 3.8 times higher than honeycomb structures. Therefore, we boldly assume that the incorporation of the TPMS structure can increase the anti-multi-shot ballistic performance. Furthermore, its elastic resistance is also better than that of the laminate structure. We then carry out finite element simulation in order to guide practical applications.

Biomimetic design of armadillo shell

The special structure of armadillos inspired the biomimetic design of armor. Figure 1c presents the configuration of an armadillo's posterior carapace[32], arranged in a regular pattern of hexagonal osseous plates connected through collagen fibers. This structure not only facilitates a degree of flexibility but also enhances the interchangeability of individual bone plates due to its compartmentalized nature. A network of fibers in the carapacal unit acts as a framework that connects the subcutaneous tissue to form the "soft layer" of the armadillo, while the keratin-rich bone shell forms the "hard layer". In the event of an attack, the hard layer responds to external penetration in the first time, whereas the soft layer provides structural support and energy absorption, thereby augmenting the protective capability. Furthermore, the protective area at the armadillo's rear is composed of multiple hexagonal shell units, combining flexibility with enhanced resistance to repeated impacts.

Inspired by the hardy layers and interpenetrating layer working principles of the armadillo, this paper addresses the issue of insufficient ballistic resistance in existing ceramic/metal laminated composite structures. It introduces a design methodology for a dense ceramic layer-porous ceramic framework featuring a three-dimensional continuous transition. This design is coupled with aluminum alloy casting to fabricate the composite armor, which consists of a dense ceramic layer, a ceramic/metal interpenetrating layer, and a metal layer following an idea outlined in Fig. 1. The entire composite armor is constructed using a closely packed arrangement of units. With ballistic resistance in mind, the upper surface of the dense ceramic layer incorporates micro-curvatures ranging from 0 to π/3. The interpenetrating layer is composed of ceramic skeleton and cast Al, which penetrate each other. The specific design ideas are shown in Fig. 1. Traditional ceramic/metal laminated composite structures utilize adhesive bonding between ceramic and metal plates. To enhance multi-hit performance and reduce maintenance costs, the current study modularizes the entire panel units. Within the interpenetrating layer, the ceramic structure is constituted by a triply periodic minimal surface (TPMS) skeleton, the zero-curvature surface topology of which is effective in mitigating the concentration of stress[33,34]. The TPMS ceramic skeleton is cohesively integrated with the dense ceramic layer to decelerate stress propagation and to effectively forestall interfacial delamination between the ceramic and metallic layers[35].

Through static compression testing and computational simulations, our research group studied the stress–strain profiles of the G-type and P-type configurations within the TPMS[36]. Results indicate that the G-type

Fig. 1. Design optimization of armadillo-inspired biomimetic composite armor.

structure endures compression with relatively uniform stress distribution, devoid of significant stress concentrations, while the P-type structure exhibits stratified stress distribution with potential stress concentrations. Consequently, the G-type structure, characterized by superior compressive strength and energy absorption properties, has been selected for the ceramic skeleton. Its structural mathematical expression is provided as follows[37]:

$$fx, y, z = \sin(\omega_x x)\cos(\omega_y y) + \sin(\omega_y y)\cos(\omega_z z) + \sin(\omega_z z)\cos(\omega_x x) = C \qquad (1)$$

$$\omega = \frac{\pi}{l} \qquad (2)$$

Here, x, y, z represent the length of the TPMS structure in three orthogonal directions respectively, ω represents the periodicity in the implicit function expression of the minimal surface, and l signifies the length of the minimal surface unit cell. C represents the level-set constant which controls the offsetting of the considered TPMS structure. In previous research, we detailed the specific generation method of the TPMS structure[36]. G-type TPMS structure is designed by implicit function. Set the numerical range and divide the interval, and the TPMS period is set to 1.5. Using the Holistic algorithm in the cross reference operator, the corresponding X, Y and Z coordinates of the model are obtained. Finally, the random distribution of coordinate points is taken as the independent variable of the function and input into the implicit function expression of G-TPMS. The isosurface is extracted by cubic algorithm, and a porous mesh structure without thickness is formed. The operation process is shown in Fig. 2.

According to Marching cube algorithm, the generated G-shaped TPMS is composed of many triangular surfaces without wall thickness, which need to be constructed with constant wall thickness by offset (this paper chooses ξ = 1 mm), and the specific parameters are shown in Fig. 3. Based on the reviewers' comments, we have carefully checked and revised the manuscript.

The parameterized TPMS structure is transformed into entity through the mesh reconstruction of STAR-CCM+ and Geomagic Wrap. Finally, through the design and transformation of UG, the composite armor structure designed in this paper is finally generated.
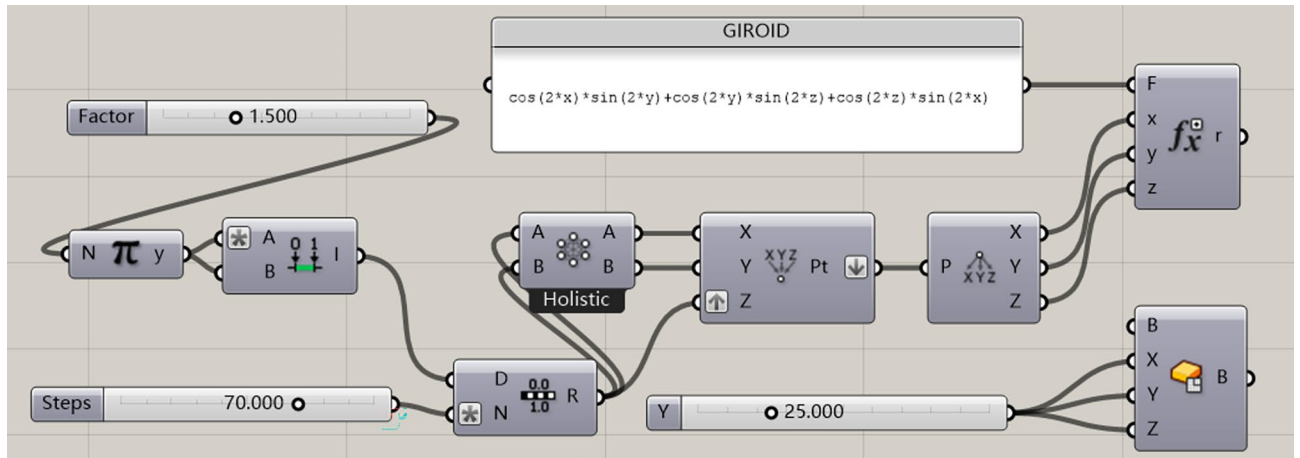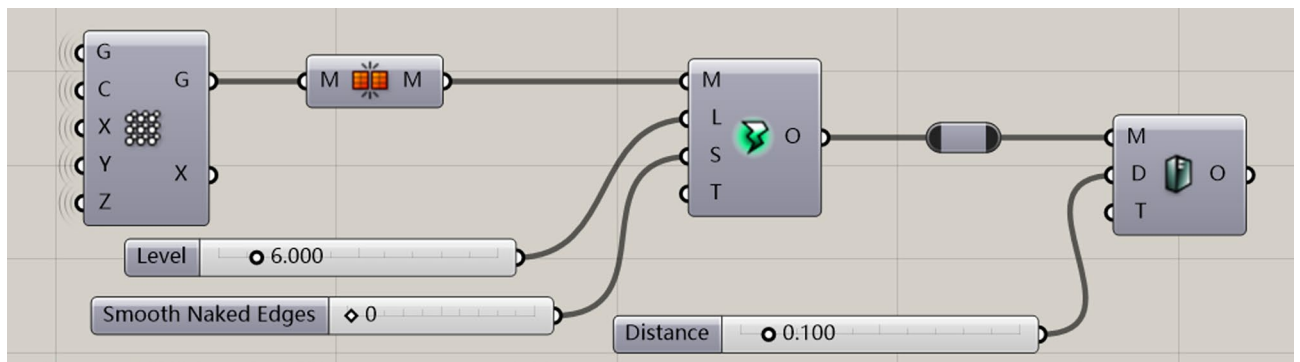
Fig. 2. G-TPMS structure design process.

Fig. 3. Post-treatment process of porous structure.

Establishment of the model

Establishment of physical model

The structure of the bio-inspired ceramic/metal composite armor unit is illustrated in Fig. 4. H_I designates a hexagonal micro-curved ceramic layer with the characteristic silhouette of an armadillo shell; H_{II} is a three-dimensional continuous interpenetrating composite structure of Al_2O_3/Al, at its skeleton is G-type TPMS structure. The dense ceramic layer and the ceramic skeleton within H_{II} are designed as an integrated whole, fabricated via 3D printing techniques; H_{III} represents an aluminum backing layer. Both H_{III} and the aluminum contained within H_{II} are cast cohesively to form a unit, whereby the entire composite armor unit envelops a TPMS-alumina ceramic skeleton within a continuous metal network structure.

The composite armor has a total thickness of 28 mm, with H_{III} comprising an 8 mm thickness, and a combined thickness of 20 mm allocated to H_I–Al_2O_3 ceramic layer and the H_{II}–Al_2O_3/Al interpenetrating layer. Three sets of structures named A, B, and C were designed based on different ratios for H_I/H_{II} as 10/10, 13.4/6.6, and 15/5,
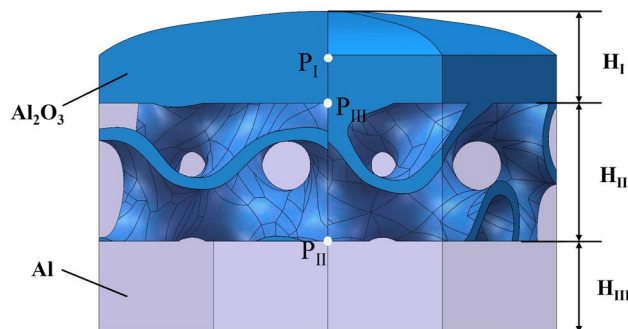

Fig. 4. Schematic diagram of the semi-section of the biomimetic composite armor structure.

respectively. Additionally, a laminated structure, referred to as structure D, served as a reference group. Detailed specifications and ratios for these configurations are listed in Table 1.

Establishment of finite element model
A computational model was developed using LS-Dyna for simulations which utilized a 7.62 mm bullet model. Given the negligible effect of the bullet casing on penetration, the analysis focused solely on the impact of a steel core on the composite armor, with the steel core itself having a diameter of 8.6 mm and a height of 24 mm. The bullet was modeled from high-strength steel with a density of 7850 kg/m³, employing the MAT_PLASTIC_KIN-EMATIC material model[38], with parameters detailed in Table 2.

Based on the analysis of grid convergence in related literature[39–42], considering the calculation efficiency and accuracy, the finite element model is determined to be SOLID164 by trial and error, and the grid size of missile body is about 1 mm, and the bullet head grid size is about 0.5 mm. In order to avoid the influence of target meshing on the numerical simulation results, the target plate was divided into 0.1 mm, 0.5 mm, 1 mm and 2 mm meshes and simulated under the condition that the size of the projectile mesh was determined. Figure 5 shows the variation curves of the residual velocity of the projectile penetration with the initial velocity of the projectile obtained by simulation under different target grid densities. The experimental curve represents the fitted curve of the residual velocity of bullets impacting on the laminated composite armor at initial velocities ranging from 600 to 1400 m/s. The laminated composite armor is prepared by adhering sintered ceramic layers produced by 3D printing and Al layers obtained through melting and casting. As can be seen from the figure, with the refinement of the grid size of the target plate, the numerical simulation results of the residual velocity of the projectile penetrating the target plate are getting closer and closer to the experimental values, and the 0.1 mm grid is the closest. In general, the simulation results converge as the mesh density increases. However, a higher mesh density will significantly increase the simulation time, so it is more reasonable to use a 0.5 mm mesh for convergence analysis in this study.

Constituencies	H$_I$/H$_{II}$ (mm)	Thickness ratio
A	10/10	1:1
B	13.4/6.6	2:1
C	15/5	3:1
D	13.4/6.6	2:1

Table 1. Structural proportions.

Property	ρ (kg/m³)	Young's modulus/GPa	Poisson's ratio	Yield stress/MPa
Bullet	7850	210	0.33	355

Table 2. Bullet material parameters.
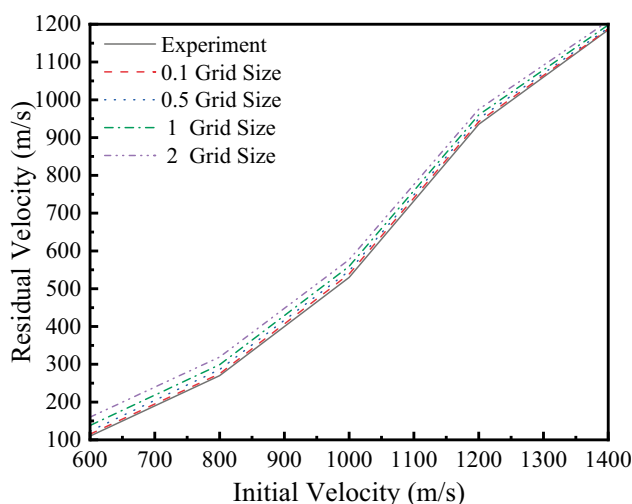
Fig. 5. The residual velocity of the projectile body under different grid sizes of the target plate varies with the initial velocity.

Commonly used alumina ceramic materials were selected for the ceramic component, with a density of 3900 kg/m³. These ceramics were characterized using MAT_JOHNSON_HOLMQUIST_CERAMICS material model, which incorporates features such as compressive strength and properties related to damage and fracture[43], with specific parameters indicated in Table 3.

Aluminum alloy was chosen for the metal material, featuring a density of 2780 kg/m³. Due to significant plastic deformation and localized high temperatures experienced by the metal plates and backing layers during penetration, the Johnson–Cook constitutive model was employed to describe these behaviors[44], with parameters included in Table 4.

Because the material strain rate is very high during bullet penetration, and the material pressure far exceeds the yield stress, in order to accurately simulate the propagation of stress wave during impact, Gruneisen equation of state is introduced[45]. Considering the complexity of the ceramic skeleton and the metal structure infiltrated through sintering, both components of the mesh were based on tetrahedral elements (SOLID187).

The JH-2 strength model constructs the corresponding relationship that ceramic strength decreases continuously with damage accumulation:

$$\sigma^* = \sigma_i^* - D\left(\sigma_i^* \sigma_f^*\right) \tag{3}$$

Among them, the stress becomes dimensionless equivalent stress through normalization under Hugoniot elastic limit state, as follows:

$$\sigma^* = \sigma / \sigma_{HEL} \tag{4}$$

The dimensionless initial strength and failure strength are as follows:

$$\sigma_i^* = A\left(P^* + T^*\right)^N \left[1 + Cln\left(\frac{\dot{\varepsilon}}{\dot{\varepsilon}_0}\right)\right] \tag{5}$$

$$\sigma_f^* = B\left(P^*\right)^M \left[1 + Cln\left(\frac{\dot{\varepsilon}}{\dot{\varepsilon}_0}\right)\right] \tag{6}$$

where A, B, C, M and N are material constants and D is damage factor ($0 < D < 1$). The damage function of JH-2 keeps accumulating damage until the damage plastic strain is reached, and the material fails. Among them, the crushing plastic strain of materials can be expressed as:

$$\varepsilon_p^f = D_1\left(P^* + T^*\right)D_2 \tag{7}$$

The pressure model is:

$$P = K_1\mu + K_2\mu^2 + K_3\mu^3 + \Delta P \tag{8}$$

where K_1, K_2 and K_3 are constants. Is the compressibility factor. When the damage begins to accumulate ($d > 0$), expansion will occur. The expansion effect is to increase the pressure and volume strain by increasing the incremental pressure p.

In the case of the simpler laminated structures, both the Al_2O_3 ceramic layer and the Al backing layer were meshed using SOLID164 elements, with a grid size of 0.5 mm. CONTACT_AUTOMATIC_SURFACE_TO_SURFACE was utilized for the contact, keeping other parameters consistent with the designated structure.

ρ (kg/m³)	G/GPa	A/MPa	B/MPa	C/MPa	M	N
3900	135	987	770	0.0	1.0	0.376
ESPI	T /GPA	Sf MAX/GPa	HEL/GPa	P_HEL/GPa	D₁	D₂
1.0	0.15	0.5	5.9	2.2	0.01	1.0
K₁/GPa	K₂/GPa	K₃/GPa	β	PSFAIL	–	–
200	0.0	0.0	1.0	–	–	–

Table 3. Material model parameters of Al_2O_3.

ρ (kg/m³)	ν	E/GPa	T_r/K	T_m/K	A/MPa	B/MPa	N
2780	0.33	73.083	300	775	369	684	0.73
C	M	C_p/J·kg⁻¹·K⁻¹	D₁	D₂	D₃	D₄	D₅
0.0083	1.7	875	0.13	0.13	− 1.5	0.011	0.0

Table 4. Aluminum alloy material parameters.

Constraints were applied to the boundaries of the composite armor units, and the interaction between the bullet and the composite armor was modeled using CONTACT_ERODING_SURFACE_TO_SURFACE. For all materials, elements were allowed to be removed to avoid computational issues related to excessively distorted elements. Deletion of elements occurred when all integration points within an element met the failure criteria defined in each material model.

Result and discussion

Determination of the optimum H_I/H_{II} thickness ratio

The variation of the residual velocity of the bullet with the initial impact velocity when the 7.62 mm bullet penetrates the composite structure with different H_I/H_{II} thickness ratios is simulated by LS-DYNA. The results are shown in Fig. 6. The residual velocity increases with the increase of the bullet impact velocity. At an impact velocity of 600 m/s, all three structures successfully resisted ballistic penetration, resulting in a residual velocity of 0, with penetration depths for structures A, B, and C measured at 21.7 mm, 14.7 mm, and 13.2 mm, respectively. When the impact velocity reached 1200 m/s, all three structures were fully penetrated, with corresponding residual velocities of 518 m/s, 220 m/s, and 226 m/s, respectively, among which the increasing trends for A and C were greater than that for B; when the impact velocity was greater than 1200 m/s, structure B exhibited a lower residual velocity than structures A and C.

Due to the different structural proportions, the resistance of different configurations is different. The numerical simulations demonstrated that the residual velocity of the bullet generally increases with the impact velocity. When the impact velocity is below 1200 m/s, increasing the ceramic thickness ratio significantly reduces the bullet's residual velocity. At an impact velocity of 1200 m/s, the relationship of residual velocities is structure A > structure C > structure B. For impact velocities above 1200 m/s, the change in bullet residual velocity is no longer directly correlated with the thickness ratio.

Different structural proportions lead to different arrival times of stress waves at different material interfaces, and due to the difference of buffer areas in H_{II}, the reflected wave intensities of different configurations are different. When the impact velocity of the projectile is 1200 m/s, the pressure change curves of the pressure test points in different structures are shown in Fig. 7. Figure (a shows the pressure evolution at testing point P_I, located on the central axis 4mm from the upper surface, while Fig. 7b represents the central point P_{II} at the interface of H_{II} and H_{III}, with both points illustrated in Fig. 4. As seen from Fig. 7a, the duration of stress sustenance for structures A, B, and C was 13 μs, 22 μs, and 20 μs, respectively. Peak pressures ranked as B > C > A, and the pressures generally increased over time until the structures failed. Because of the proper proportion, the structure B makes the propagation of stress wave in H_I more delayed than the other two. The complex and efficient TPMS structure in H_{II} makes the downward transmitted stress wave constantly resisted and eliminated, while the other two structure are also performing this operation, but the efficiency is low. In Fig. 7b, structure A displayed the highest peak pressure (− 198.3 MPa) and the shortest resistance duration (31.4 μs). Structure B consistently experienced lower stresses than structure C, and its interfacial pressure variation was also significantly less than that of structure C. At the 32 μs mark in Fig. 7b, stress concentration was observed at point P_{II} in structure A, with opposing pressures noted between peripheral and central regions indicative of shear phenomena. Pressure in structures B and C appeared more dispersed. The results suggest that under high-velocity impacts, compared to the stress concentration in structure A and higher average pressures in structure C, structure B excelled in dissipating and attenuating the stress waves at the H_{II}/H_{III} interface, which in turn provided superior support for the top ceramic layer, resulting in the highest pressure peak and the longest penetration resistance time near point P_I. Considering the relationship between residual velocities and impact speeds in relation to areal density requirements shown in Fig. 7, we infer that structure B, which has a thickness ratio of 2:1, offers superior ballistic protection over the other thickness ratios. This is consistent with the conclusions in the literature[41].
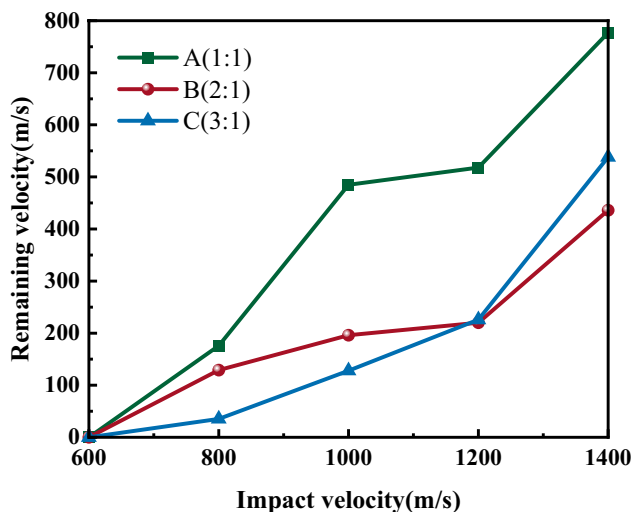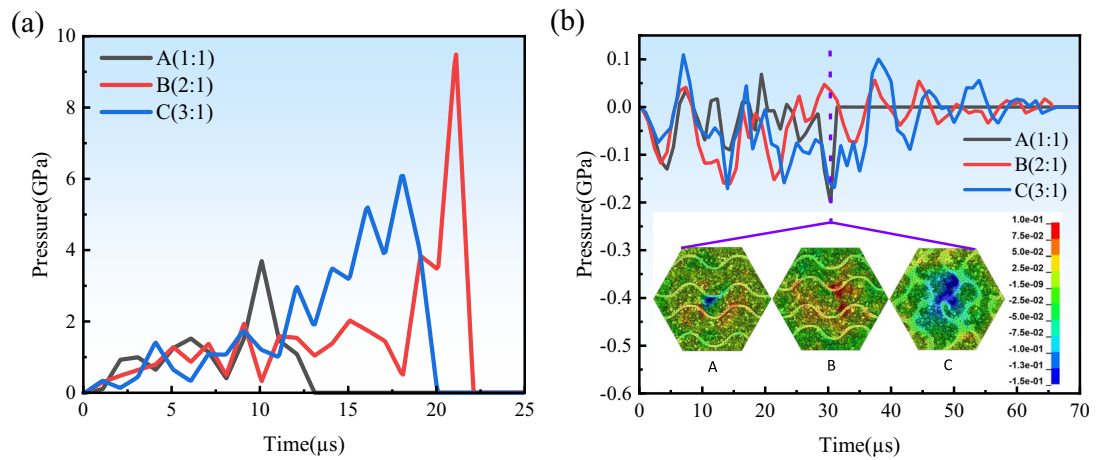

**Fig. 6.** The law of residual velocity of bullet changing with initial impact velocity.

Fig. 7. (**a**) Pressure–time curves of point P_I of different structures at 1200 m/s; (**b**) The pressure time curves of point P_{II} of different structures at 1200 m/s and the stress contours of each structure at 32 µs.

Based on the 2:1 thickness ratio design, TPMS skeletal parameters (period and wall thickness) were adjusted to yield frameworks with porosities of 88%, 82%, and 72%, creating corresponding bio-inspired ceramic/metal composite armor units. Subjecting these three models to 7.62 mm bullet penetrations at an initial velocity of 700 m/s, the velocity–time curves along the Z-direction of the bullet are displayed in Fig. 8. The results reveal that the structure with 82% porosity exhibited the most significant decrease in velocity (700 m/s) compared to the other two models (530 m/s and 616 m/s), achieving complete protection only at 82% porosity, thereby demonstrating optimal ballistic resistance.

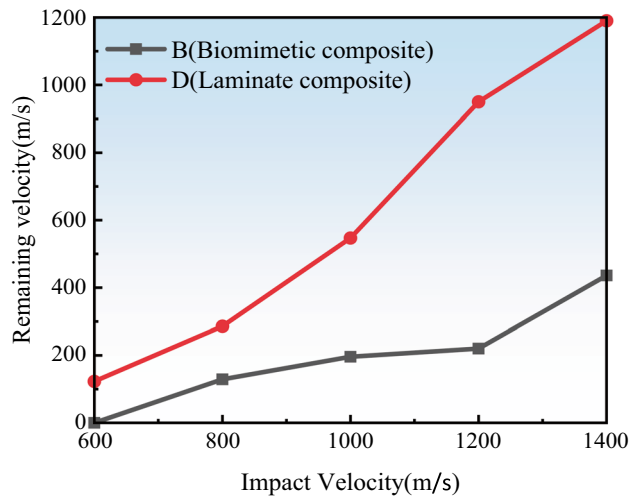## Anti-ballistic performance of two kinds of composite armor unit

Literature has confirmed that a H_I/H_{II} ratio of 2 is the optimal thickness ratio for ceramic/metal laminated composite structures[43]. Figure 9 depicts the comparative results of the residual velocities of bullets at different penetration velocities for the biomimetic composite structure (structure B) with a H_I/H_{II} thickness ratio of 2:1 and the laminated structure (structure D). At the same initial impact speeds, the residual velocity of structure D is consistently higher than that of structure B; moreover, as the penetration initial velocity increases, the residual velocities for both structures B and D exhibit an upward trend, although the increase for structure B is less than that of structure D.

Employing a 7.62 mm steel-core pistol projectile as the focus of our investigation, we established the projectile's trajectory at a normal incidence angle (0°) and an initial speed of 600 m/s, targeting penetration of structures B and D. The penetration kinetics of the bullet through structure B are elucidated in Fig. 9a, portraying the protective mechanism of the biomimetic composite armor unit across three distinct stages.
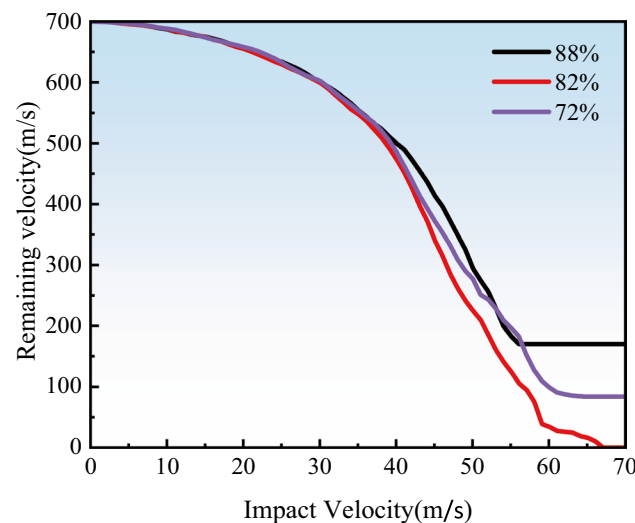
Fig. 8. The velocity time history curves of bullet penetrating different pore configurations.

8

Fig. 9. Comparison of anti-ballistic properties of two kinds of composite structures.

Stage I (0–78 µs): the bullet's velocity drops from 600 m/s to around 176 m/s, during which the reverse acceleration gradually increases to a peak of -1.08×10^7 m/s² before rapidly decreasing. This stage is the resistance phase of the H_I–Al_2O_3 ceramic layer to bullet penetration. Al_2O_3 possesses high compressive strength and hardness, which during penetration absorbs the kinetic energy of the bullet, causing brittle failure and continuously blunting and fragmenting the bullet. The Al_2O_3 layer does not experience significant indentation deformation during penetration, and its protective role ceases after being completely pierced by the bullet.

Stage II (78–106 µs): the bullet's velocity reduces from 176 m/s to approximately 64.3 m/s, where due to material differences, the reverse acceleration rapidly falls. Nonetheless, the ceramic structures within the H_{II}–Al_2O_3/Al interpenetrating layer continue to fragment the bullet, while Al encapsulates the fragments and absorbs bullet energy through yield deformation. In this stage, the bullet's reverse acceleration exhibits oscillating growth, as the bullet's kinetic energy is transformed into the deformation energy of Al, until the tensile stress exceeds the ultimate tensile strength of Al, leading to fracture and failure.

Stage III (106–135 µs): After 106 µs, both the bullet's velocity and reverse acceleration decline to zero. The bullet's remaining kinetic energy is entirely converted into the deformational energy of the Al layer, deepening the indentation depth of the Al layer.

The velocity changes of the bullets penetrating both composite structures are shown in Fig. 10b. It is evident from Fig. 10b that, under identical penetration conditions, the Al_2O_3/Al biomimetic composite armor unit reduces the bullet's residual velocity to 0 within 132 µs, whereas the Al_2O_3/Al laminated composite structure is penetrated, with a residual velocity of 123 m/s. In stage A (0–45 µs), since both structures have the same projectile-facing surface, the initial acceleration and velocity are relatively similar; in stage B (45–78 µs), because the laminate H_{II} can only attenuate and reflect the stress wave of the foundation, while the biomimetic composite unit destroys and decomposes the stress wave through the complex TPMS ceramic-Al interface, the elastic resistance of each unit is different in the process of stage B, the resultant tensile reflective wave damage varies, resulting in a higher acceleration for the biomimetic structure compared to the laminated one; in stage C (78–130 µs), the
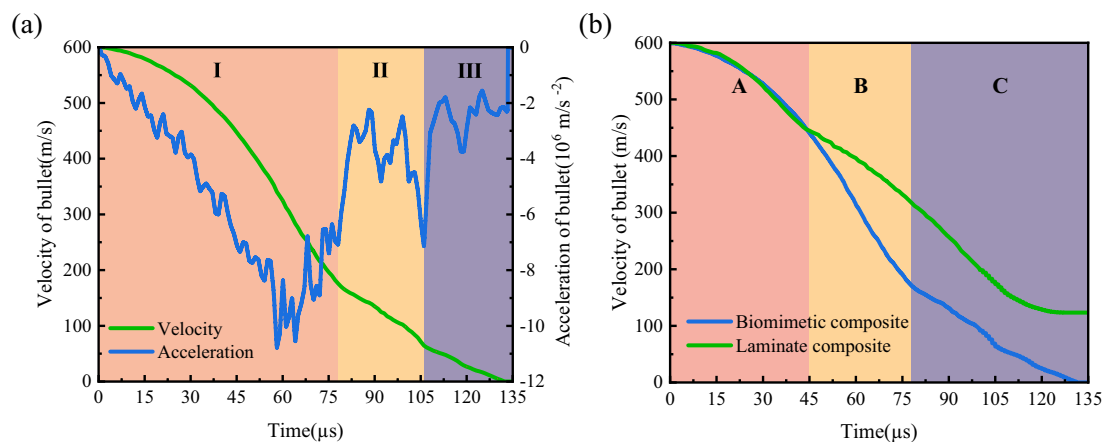

Fig. 10. (**a**) Velocity and acceleration-time history curve of 7.62 mm steel pistol bullet in the Z direction; (**b**) comparison of the velocity changes of bullets penetrating different structures.

bullet that penetrated the laminated structure retained higher residual velocity and punched through the back-plate, while the Al_2O_3/Al biomimetic composite armor unit successfully resisted penetration. Overall, throughout the entire bullet penetration process, the structure designed in this study exhibits superior ballistic resistance.

To explain clearly how different structures result in varying speed variations in stage B, we have analyzed the pressure at the center point P_{III} between the H_I layer and the H_{II} layer depicted in Fig. 3, specifically when the bullet, traveling at an initial velocity of 600 m/s, penetrates structures B and D, as further illustrated in Fig. 11. The pressure endured by structure B is weaker than that of structure D within 0–30 µs and displays a cyclical pattern of increase–decrease corresponding to pressurization and depressurization cycles. Combining the analysis of the pressure variation curve of structure B from Fig. 7, we infer that most of the stress at the interface in structure B is conducted to the interpenetrating layer. On the other hand, in structure D, due to the impedance mismatch at the interface, the stress wave is not effectively transmitted downward and attenuated, leading to a continuous accumulation of pressure until failure.

The equivalent stress nephogram of bullet penetrating Al_2O_3/Al composite armor is shown in Fig. 12a–d. As shown in Fig. 12a, a spherical stress wave is generated near the impact point at the center due to high kinetic energy and high compressive stress, which extends towards the back surface of the ceramic plate. As the stress wave propagates from the dense ceramic layer to the interface between the two materials, the incident wave is divided into transverse transmission and reflection waves due to the difference in wave impedance. These reflection waves interact with the incoming and outgoing pressure loading waves, creating localized tension or shear near the interface, as depicted in Fig. 12b. When the tensile stress exceeds the material's strength limit, cracks form, originating from the back surface of the H_I–Al_2O_3 ceramic layer towards the contact surface, converging with conical cracks to form a complete ceramic cone, allowing the bullet to continue penetrating into the metal layer until breakthrough, as shown in Fig. 12c, d.
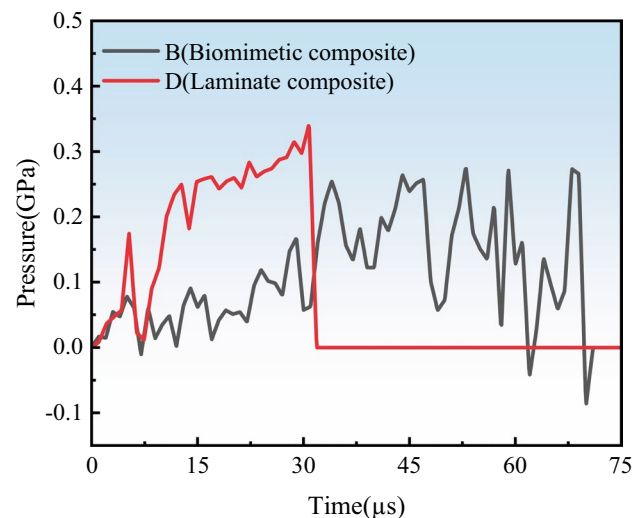
Fig. 11. P_{III} point pressure–time curve of a laminate and a biomimetic composite structure at 600 m/s.
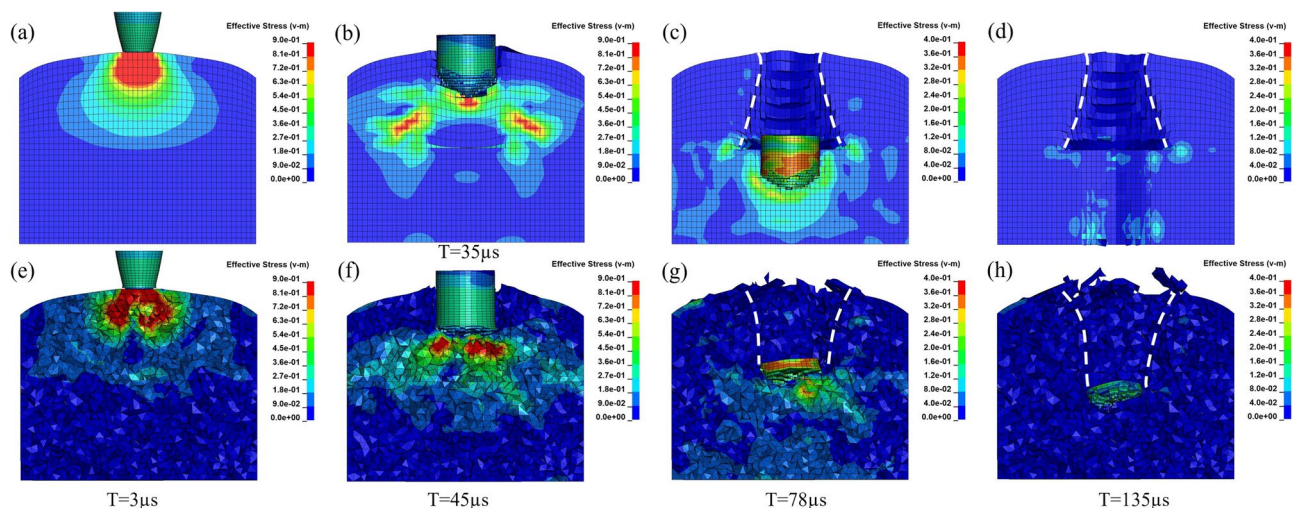
Fig. 12. Stress contours of two types of target plate penetration processes.

The equivalent stress contour for the bullet penetrating the Al_2O_3/Al biomimetic composite armor, as observed in Fig. 12e–h. At the same penetration depth, the stress diffusion zone and intensity in the biomimetic composite armor are lower than in the laminated composite armor. Compared to the shear stress concentration caused by the stress waves in the laminated composite armor shown in Fig. 12b, the biomimetic composite armor in Fig. 12f only exhibits stress concentration in the penetration zone, with the effects of stress waves tending to disperse. Furthermore, as shown in Fig. 12g, h, due to the existence of numerous complex TPMS interfaces between the ceramic and metal phases in the interpenetrating layers, the stress waves are significantly attenuated while propagating in a dispersed manner. This, along with the different instantaneous forces acting on the bullet, leads to the bullet's deflection.

Comparing the entire penetration duration equivalent stress contour for both structures reveals that the ceramic layer damage in the biomimetic composite armor is less than that in the laminated composite armor, with ceramic cone formation being suppressed. The monolithic formation of the dense ceramic layer with the TPMS lattice in the biomimetic composite armor allows the stress wave to continue propagating downward and attenuating after reaching the interface, further scattering and reducing the reflective stress wave damage at the H_I and H_{II} interface. The transmitted waves in the interpenetrating structure are continuously reflected and absorbed by the TPMS structure, resulting in diminished stress wave transfer downward compared to the laminated structure, thereby reducing damage and deformation to the lower backplate. Additionally, the inclusion of the TPMS ceramic lattice not only accelerates bullet fragmentation but also achieves a yawing effect, altering the force application points of the bullet penetration and inducing bullet deflection, which to some extent delays the bullet penetration behavior. Layer H_I of biomimetic composite armor unit also cracked and shattered, but the damage degree was obviously less than that of laminated composite unit. In the later penetration process, Al_2O_3/Al biomimetic composite armor had a better damage reduction effect on bullets. With the addition of TPMS skeleton, the difference of interface wave impedance becomes larger. TPMS structure can optimize the stress distribution in the whole target area, thus improving deformation compatibility, which delays and reduces the development of radial and circumferential cracks, which increases the wear effect between ceramics and projectiles and improves the ability to hinder projectile propulsion. In conclusion, the bullet-resistant capability of the Al_2O_3/Al biomimetic composite armor is superior to that of the laminated composite armor.

Conclusion

In this study, inspired by the structural characteristics of the armadillo shell, we perform numerical simulations to investigate the ballistic resistance of Al_2O_3/Al biomimetic composite armor cells with varying thickness ratios, benchmarking them against conventional laminated composite armor. The investigation substantiates that ceramic/metal biomimetic composite armor configurations exhibit superior ballistic resistance. An optimized design of the Al_2O_3/Al biomimetic composite cell structure is achieved with an overall thickness of 28 mm. The salient conclusions drawn are as follows:

(1) Inspired by the armadillo armor structure, we designed a new type of Al_2O_3/Al biomimetic composite armor with continuous interpenetrating characteristics. Based on existing TPMS research, this paper develops the design process for this composite armor, studies the influence of design parameters on its ballistic resistance, and identifies the optimal model.
(2) Computer simulations reveal that Al2O3/Al biomimetic composite armor mitigates interface acoustic impedance mismatch through structural design, effectively disperses and attenuates stress waves, thereby enhancing ballistic performance. Its modular design facilitates easy replacement, enhances cost-effectiveness in protection, and is ideal for lightweight defense applications.
(3) Under the penetration of a bullet with an initial velocity of 600 m/s, the biomimetic composite structure achieved complete protection with a penetration depth of only 14.7 mm, compared to the same thickness laminated composite structure which was fully penetrated with a residual bullet velocity of 123 m/s. When the thickness ratio of the ceramic layer to the interpenetrating layer is 2:1, the biomimetic composite armor unit possesses the optimal ballistic resistance.
(4) Simulation results demonstrate that the Al2O3/Al biomimetic ceramic/metal interpenetrating phase effectively inhibits crack propagation by deflecting projectiles and inducing ductile deformation in metal materials. The alternating ceramic and metal interfaces disperse and weaken stress waves. Complex stress wave reflection and transmission behaviors delay the peak time of reflected tensile waves, prolong projectile-armor interaction time, and enhance armor's kinetic energy dissipation capacity.

Data availability

The data supporting the findings of this study are available from the corresponding author upon reasonable request. Data is provided within the manuscript or supplementary information files.

References

1. Du, S. Q. *et al.* Study on the protective performance of high-performance multi-scale (SiCh-p+B4Cp)/5083Al ceramic array armor with excellent ballistic properties. *J. Market. Res.* **27**, 6756–6768. https://doi.org/10.1016/j.jmrt.2023.11.125 (2023).
2. Zhai, Y. X., Wu, H. & Fang, Q. Interface defeat studies of long-rod projectile impacting on ceramic targets. *Def. Technol.* **16**, 50–68. https://doi.org/10.1016/j.dt.2019.05.021 (2020).

3. Hu, Q.-R., Shen, X.-Y., Qian, X.-M., Huang, G.-Y. & Yuan, M.-Q. The personal protective equipment (PPE) based on individual combat: A systematic review and trend analysis. *Def. Technol.* **28**, 195–221. https://doi.org/10.1016/j.dt.2022.12.007 (2023).

4. Xu, H. *et al.* In-situ synthesis and low-temperature fabrication of B₄C/TiB₂-based multilayer graded composites with B₄C and Ti–Al intermetallics mixtures through transient liquid phase sintering. *Ceram. Int.* **47**, 24384–24392. https://doi.org/10.1016/j.ceramint.2021.05.152 (2021).

5. Guo, W., Bai, S. & Ye, Y. Controllable fabrication and mechanical properties of C/C–SiC composites based on an electromagnetic induction heating reactive melt infiltration. *J. Eur. Ceram. Soc.* **41**, 2347–2355. https://doi.org/10.1016/j.jeurceramsoc.2020.11.018 (2021).

6. Tan, M. T., Zhang, X. F., Goh, W. L., Luo, B. Y. & Bao, K. Study on transition from dwell/interface defeat to penetration of long-rod projectile impacting silicon carbide. *Int. J. Fract.* **219**, 65–87. https://doi.org/10.1007/s10704-019-00379-5 (2019).

7. Gilson, L., Coghe, F., Bernardi, A., Imad, A. & Rabet, L. Ballistic limit evolution of field-aged flexible multi-ply UHMWPE-based composite armour inserts. *Compos. Struct.* **322**, 117414. https://doi.org/10.1016/j.compstruct.2023.117414 (2023).

8. Zhang, B. *et al.* An analysis of bi-layer ceramic armor and optimization of protection efficiency. *Mater. Des.* **203**, 109633. https://doi.org/10.1016/j.matdes.2021.109633 (2021).

9. Aydin, M. & Soydemir, M. Ballistic protection performance of a free ceramic particle armor system: An experimental investigation. *Ceram. Int.* **47**, 11628–11636. https://doi.org/10.1016/j.ceramint.2020.12.295 (2021).

10. Batra, R. C. & Pydah, A. Impact analysis of PEEK/ceramic/gelatin composite for finding behind the armor trauma. *Compos. Struct.* **237**, 111863. https://doi.org/10.1016/j.compstruct.2020.111863 (2020).

11. Guo, X. *et al.* Simulation of ballistic performance of a two-layered structure of nanostructured metal and ceramic. *Compos. Struct.* **157**, 163–173. https://doi.org/10.1016/j.compstruct.2016.08.025 (2016).

12. Zhang, D., Guo, D., Wang, F., Dong, H. & Wang, Z. Low-velocity impact response of a novel bionic turtle shell back armor sandwich structure. *J. Mater. Res. Technol.* **29**, 910–923. https://doi.org/10.1016/j.jmrt.2024.01.176 (2024).

13. Lin, J., Li, Y., Liu, S. & Fan, H. Numerical investigation of the high-velocity impact performance of body armor panels. *Thin-Walled Struct.* **189**, 110909. https://doi.org/10.1016/j.tws.2023.110909 (2023).

14. Signetti, S., Ryu, S. & Pugno, N. M. Impact mechanics of multilayer composite armors: Analytical modeling, FEM numerical simulation, and ballistic experiments. *Compos. Struct.* **297**, 115916. https://doi.org/10.1016/j.compstruct.2022.115916 (2022).

15. Kota, N., Charan, M. S., Laha, T. & Roy, S. Review on development of metal/ceramic interpenetrating phase composites and critical analysis of their properties. *Ceram. Int.* **48**, 1451–1483. https://doi.org/10.1016/j.ceramint.2021.09.232 (2022).

16. Almesmari, A., Alagha, A., Naji, M. M., Sheikh-Ahmad, J. & Jarrar, F. Recent advancements in design optimization of lattice-structured materials. *Adv. Eng. Mater.* **25**, 2201780 (2023).

17. Wang, Y. *et al.* Improved ballistic performance of a continuous-gradient B₄C/Al composite inspired by nacre. *Mater. Sci. Eng. A* **874**, 145071. https://doi.org/10.1016/j.msea.2023.145071 (2023).

18. Chao, Z. L. *et al.* The microstructure and ballistic performance of B4C/AA2024 functionally graded composites with wide range B4C volume fraction. *Compos. Part B Eng.* **161**, 627–638. https://doi.org/10.1016/j.compositesb.2018.12.147 (2019).

19. Kota, N., Jana, P., Sahasrabudhe, S. & Roy, S. Processing and characterization of Al-Si alloy/SiC foam interpenetrating phase composite. *Mater. Today Proc.* **44**, 2930–2933. https://doi.org/10.1016/j.matpr.2021.01.923 (2021).

20. Prasanth, A. S. *et al.* Uniaxial compressive behavior of AA5083/SiC Co-continuous ceramic composite fabricated by gas pressure infiltration for armour applications. *J. Compos. Sci.* https://doi.org/10.3390/jcs6020036 (2022).

21. Lu, J. *et al.* Mechanical properties of Al₂O₃ and Al₂O₃/Al with gyroid structure obtained by stereolithographic additive manufacturing and melt infiltration. *Ceram. Int.* **48**, 23051–23060. https://doi.org/10.1016/j.ceramint.2022.04.283 (2022).

22. Chang, H. *et al.* High strain rate characteristics of 3–3 metal–ceramic interpenetrating composites. *Mater. Sci. Eng. A* **528**, 2239–2245. https://doi.org/10.1016/j.msea.2010.12.016 (2011).

23. Pan, G., Su, H., Li, X. & Wang, J. Coupled FEM-SPH simulation of the protective properties for metal/ceramic composite armor. *Int. J. Lightweight Mater. Manuf.* **6**, 543–551. https://doi.org/10.1016/j.ijlmm.2023.05.007 (2023).

24. Kong, D. *et al.* Method for preparing biomimetic ceramic structures with high strength and high toughness. *Ceram. Int.* **49**, 40284–40296. https://doi.org/10.1016/j.ceramint.2023.10.001 (2023).

25. Ghanbari, J. & Panirani, P. N. A hybrid bio-inspired sandwich structures for high strain rate energy absorption applications. *Sci. Rep.* **14**, 2865. https://doi.org/10.1038/s41598-024-53521-2 (2024).

26. Cho, B., Kim, D. & Kim, T. Exceptional properties of hyper-resistant armor of a hydrothermal vent crab. *Sci. Rep.* **12**, 11816. https://doi.org/10.1038/s41598-022-15982-1 (2022).

27. Islam, M. K., Hazell, P. J., Escobedo, J. P. & Wang, H. Biomimetic armour design strategies for additive manufacturing: A review. *Mater. Des.* **205**, 109730. https://doi.org/10.1016/j.matdes.2021.109730 (2021).

28. Du Plessis, A., Broeckhoven, C., Yadroitsev, I., Yadroitsava, I. & Le Roux, S. G. Analyzing nature's protective design: The glyptodont body armor. *J. Mech. Behav. Biomed. Mater.* **82**, 218–223 (2018).

29. Lazarus, B. S., Velasco-Hogan, A., Gómez-del Río, T., Meyers, M. A. & Jasiuk, I. A review of impact resistant biological and bioinspired materials and structures. *J. Mater. Res. Technol.* **9**, 15705–15738. https://doi.org/10.1016/j.jmrt.2020.10.062 (2020).

30. Guo, G., Alam, S. & Peel, L. D. Numerical analysis of ballistic impact performance of two ceramic-based armor structures. *Compos. Part C Open Access* **3**, 100061. https://doi.org/10.1016/j.jcomc.2020.100061 (2020).

31. Zhang, F. *et al.* Quasi-static compressive fracture behavior of three-period minimum surface Al₂O₃/Al composites fabricated by stereolithography. *J. Mater. Res. Technol.* **30**, 4950–4960. https://doi.org/10.1016/j.jmrt.2024.04.224 (2024).

32. Miranda, P., Pajares, A. & Meyers, M. A. Bioinspired composite segmented armour: Numerical simulations. *J. Mater. Res. Technol.* **8**, 1274–1287. https://doi.org/10.1016/j.jmrt.2018.09.007 (2019).

33. Deng, Z.-L. *et al.* Mechanical and degradation properties of triply periodic minimal surface (TPMS) hydroxyapatite & akermanite scaffolds with functional gradient structure. *Ceram. Int.* **49**, 20808–20816. https://doi.org/10.1016/j.ceramint.2023.03.213 (2023).

34. Ejeh, C. J., Barsoum, I., Abou Ali, A. M. & Abu Al Rub, R. K. Combining multiple lattice-topology functional grading strategies for enhancing the dynamic compressive behavior of TPMS-based metamaterials. *J. Mater. Res. Technol.* **27**, 6076–6093 (2023).

35. Wang, Q., Chen, Z. & Chen, Z. Design and characteristics of hybrid composite armor subjected to projectile impact. *Mater. Des.* **46**, 634–639. https://doi.org/10.1016/j.matdes.2012.10.052 (2013).

36. Liu, S. *et al.* Parametric design and performance study of continuous gradient triply periodic minimal surface bone scaffold. *IJB* https://doi.org/10.36922/ijb.2306 (2024).

37. Rajagopalan, S. & Robb, R. A. Schwarz meets Schwann: Design and fabrication of biomorphic and durataxic tissue engineering scaffolds. *Med. Image Anal.* **10**, 693–712 (2006).

38. Zhu, D. J. & Tang, X. Experimental testing and finite element simulation of SiC-ultrahigh molecular weight polyethylene flexible protective plate inspired by armadillo shell. *Acta Mater. Compos. Sin.* **37**, 2561. https://doi.org/10.13801/j.cnki.fhclxb.20200121.001 (2020).

39. Chao, H., Huang, Z., Ren, X., Wang, J. & Li, Y. Finite element simulation of the penetration resistance of topological interlocking ceramic/PE laminates. *Compos. Struct.* **311**, 116802. https://doi.org/10.1016/j.compstruct.2023.116802 (2023).

40. Wei, Z. & Xu, X. FEM simulation on impact resistance of surface gradient and periodic layered bionic composites. *Compos. Struct.* **247**, 112428. https://doi.org/10.1016/j.compstruct.2020.112428 (2020).

41. Si, P., Bai, F., Liu, Y., Yan, J. & Huang, F. Ballistic performance of ceramic/metal composite armor systems with different thickness ratios. *Acta Armament.* **43**, 2318–2329. https://doi.org/10.12382/bgxb.2021.0844 (2022).

42. Krishnan, K., Sockalingam, S., Bansal, S. & Rajan, S. D. Numerical simulation of ceramic composite armor subjected to ballistic impact. *Compos. Part B Eng.* **41**, 583–593. https://doi.org/10.1016/j.compositesb.2010.10.001 (2010).
43. Rathod, S., Tiwari, G. & Chougale, D. Ballistic performance of ceramic–metal composite structures. *Mater. Today Proc.* **41**, 1125–1129. https://doi.org/10.1016/j.matpr.2020.08.759 (2021).
44. Buyuk, M., Kurtaran, H., Marzougui, D. & Kan, C. D. Automated design of threats and shields under hypervelocity impacts by using successive optimization methodology. *Int. J. Impact Eng.* **35**, 1449–1458 (2008).
45. Medina, S. F. & Hernandez, C. A. General expression of the Zener–Hollomon parameter as a function of the chemical composition of low alloy and microalloyed steels. *Acta Mater.* **44**, 137–148 (1996).

Acknowledgements

Author contributions

F.Z.: data curation, investigation, methodology, writing-original draft. P.Z.: formal analysis, investigation, writing-original draft. P.Lu.: conceptualization, formal analysis, validation. k.Q.: formal analysis, software, validation. S.Liu.: data curation, resources, review & editing. L.W.: formal analysis, review & editing. All authors reviewed the manuscript.

Competing interests

The authors declare no competing interests.

Additional information

Correspondence and requests for materials should be addressed to S.L.

Reprints and permissions information is available at www.nature.com/reprints.

Publisher's note Springer Nature remains neutral with regard to jurisdictional claims in published maps and institutional affiliations.